Observations of fracture propagation during decameter-scale hydraulic fracturing experiments

Conference Paper · June 2018

CITATIONS
3

READS
519

8 authors, including:

Nathan Dutler
RWTH Aachen University
30 PUBLICATIONS **428** CITATIONS
SEE PROFILE

Benoît Valley
Université de Neuchâtel
120 PUBLICATIONS **1,592** CITATIONS
SEE PROFILE

Valentin Gischig
ETH Zurich
119 PUBLICATIONS **2,161** CITATIONS
SEE PROFILE

Mohammadreza Jalali
RWTH Aachen University
115 PUBLICATIONS **774** CITATIONS
SEE PROFILE

ARMA 18-0256

Observations of fracture propagation during decameter-scale hydraulic fracturing experiments

Dutler, N. O., Valley, B.
Center for Hydrogeology and Geothermics, University of Neuchâtel, Neuchâtel, Switzerland
Gischig, V.
CSD Engineers, Bern, Switzerland
Jalali, M.R., Doetsch, J., Krietsch, H., Villiger*, L.
*SCCER-SoE / *Swiss Seismological Service, ETH Zurich, Zurich, Switzerland*
Amann, F.
Chair of Engineering Geology and Environmental Management, RWTH Aachen, Aachen, Germany

This paper was prepared for presentation at the 52nd US Rock Mechanics / Geomechanics Symposium held in Seattle, Washington, USA, 17–20 June 2018. This paper was selected for presentation at the symposium by an ARMA Technical Program Committee based on a technical and critical review of the paper by a minimum of two technical reviewers. The material, as presented, does not necessarily reflect any position of ARMA, its officers, or members. Electronic reproduction, distribution, or storage of any part of this paper for commercial purposes without the written consent of ARMA is prohibited. Permission to reproduce in print is restricted to an abstract of not more than 200 words; illustrations may not be copied. The abstract must contain conspicuous acknowledgement of where and by whom the paper was presented.

ABSTRACT:

Various in-situ hydraulic fracturing experiments were carried out in the naturally fractured, crystalline rock mass of the Grimsel Test Site (GTS) in Switzerland. The purpose was to study the geometry of the newly created fractures and their interaction with the pre-existing fracture network using transient pressure and rock mass deformation observations. Under controlled conditions, six hydraulic fractures with similar injection protocols were executed in two sub-vertical injection boreholes. The rock mass is intersected by two E-W striking shear zones (S3), and two biotite-rich meta-basic dykes with a densely fractured zone in between. The S3 shear-zone intersecting the rock volume of interest acts as a high-permeability connection to the tunnel for the experiments executed south of it. Strong variation in injectivity enhancement, jacking pressure, break down pressure, instantaneous shut-in pressure and fluid flow recovery among the different injection intervals indicate different stress conditions north and south of S3.

1. INTRODUCTION

The main requirement for extracting energy from the subsurface is sufficient fluid flow through permeable pathways to transport heat or oil/gas from the underground to a production well. The crustal permeability decreases with depth (Manning & Ingebritsen, 1999; Rutqvist & Stephansson, 2003), which influences the productivity in a negative manner. Thus, the permeability in deep target reservoirs has to be enhanced through hydraulic stimulation. Only by enhancing the permeability of the underground, sufficient conductivity and connectivity are achieved. Geothermal projects utilizing permeability enhancement techniques are referred as enhanced geothermal systems (EGS) (Cummings & Morris, 1979).

Two main processes are typically invoked during permeability enhancement: 1) hydraulic fracturing and 2) hydraulic shearing. Hydraulic fracturing is the initiation and propagation of tensile (mode I) fractures. It occurs when tensile stress exceeds tensile strength and the energy, which is required to create new surfaces in the rock exceeds fracture toughness (Detournay, 2016). When the stimulation operation is completed, the newly formed hydraulic fractures keep a residual aperture resulting in permeability enhancement (Jalali et al., 2018).

Hydraulic shearing is associated with the shear reactivation along a pre-existing discontinuity in direction of maximum in-situ shear stress on the fracture plane (Gischig & Preisig, 2015; Pine & Batchelor, 1984). Associated with fracture slip, shear dilation increases the permeability of natural fractures. This process is referred as the self-propping mechanism and is assumed to be permanent (McClure & Horne, 2014). Although these concepts are conceptually and theoretically well understood, their interactions and relative importance during hydraulic stimulation are debated. Our limitations in quantifying their respective effects prevent our ability to anticipate rock mass response to hydraulic stimulation and thus to propose a rational for hydraulic stimulation design. In addition, the quantitative relationships between these stimulation mechanisms and induced seismicity are currently poorly understood, posing a risk management issue for hydraulic stimulation operations (Eaton & Igonin, 2018).

Data sets obtained from full-scale field stimulation operations (Evans et al., 2012; McClure & Horne, 2014) provide valuable information, but limited access to the

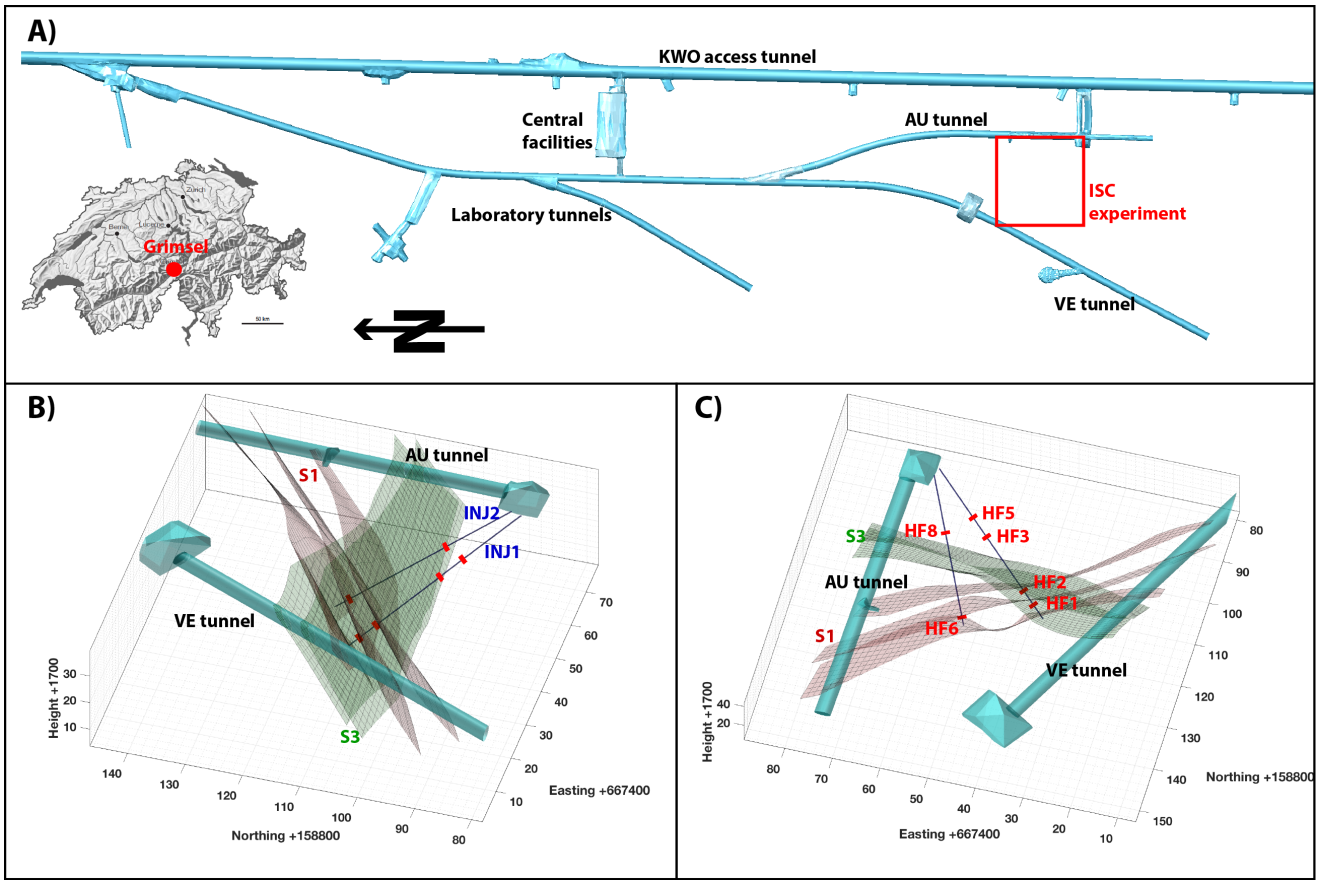

Fig 1: A) Map view of the GTS facilities with the ISC experiment located at the southern part of the GTS between AU and VE tunnels. **B)** The ISC experiment is intersected by two sets of major features S1 and S3 shear-zone. The two injection boreholes INJ1 and INJ2 are shown, too. **C)** View showing the position of the six hydraulic fracturing tests performed. Coordinates on figure B) and C) are given in Swiss metric coordinate system (CH1903).

reservoir volume prevents conclusive assessments of the detailed rock mass response.

This motivates the execution of well-controlled in-situ hydraulic fracturing experiments with extensive access to the experimental volume. Only a few of such experiments were performed so far and they provided invaluable insights into the details of rock mass response to hydraulic injections. The mine back experiment at the Nevada test site showed complex fractures shapes due to pressure and fluid distribution (Warpinski, 1985). At Northpark mine, fracture growth in naturally fractured rock was studied. The fracture geometries were studied from microseismcity and tilt data and were mapped after backmining (Jeffrey et al., 2009). The results obtained in these studies illustrated the dominant control of 1) the stress state on the overall geometry of stimulated volume and 2) the pre-existing fracture network on the development of flow path. An experiment was carried out in 2015 at the Aspö hard rock laboratory (López-Comino et al., 2017; Zang et al., 2017) to test alternative water injection schemes (continuous, progressively increasing and cyclic pressurization) in crystalline rock with various monitoring systems.

These experiments showed that site specific conditions (e.g., rock type, natural fracturing, stress state, etc.) have a major influence on the rock mass response. This motivated us to perform the In-Situ Stimulation and Circulation experiment (ISC-experiment). This decameter-scale experiment aimed to investigate in great detail rock mass responses (i.e., during both hydroshearing and hydrofracturing), as well as fluid circulation in moderately fractured granitic rocks. We performed this experiment at the Grimsel Test Site (GTS), Switzerland. The granitic rock mass in the GTS is a suitable analogue of the crystalline basement in the Alpine foreland basin and can act as a proxy for potential future EGS sites (Amann et al., 2018). A detailed rock mass characterization, including geological, hydrological and geophysical prospecting of the experimental rock volume took place prior to stimulation. The main experiment consisted of six hydraulic shearing and six hydraulic fracturing experiments.

Six hydraulic fracturing (HF) experiments were conducted to study 1) the geometry of new created fractures, 2) their interaction with the natural fracture system, 3) the response of the rock mass at different injection locations and 4) the influence of different injection metrics (e.g. fluid viscosity). HF can propagate

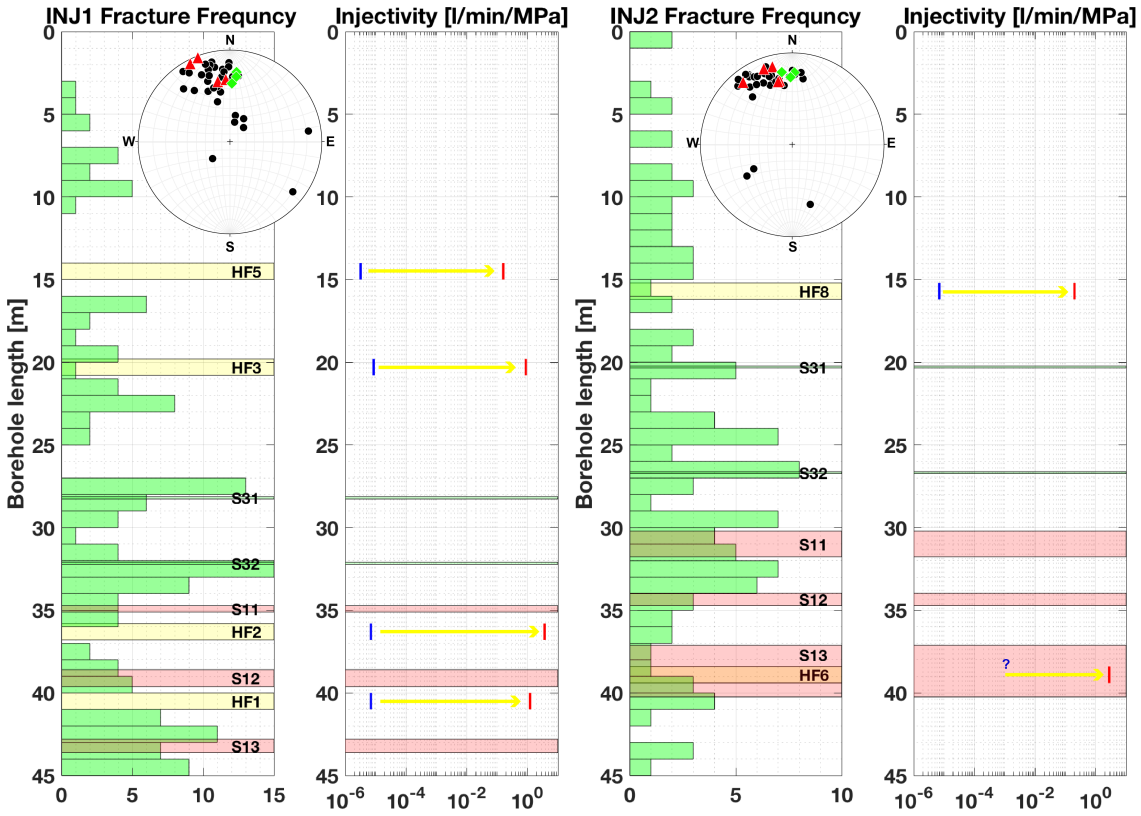

Fig 2: Fracture frequency incl. lower hemisphere equal-angle stereonet and injectivity for INJ1 and INJ2 borehole. The location of the shear-zone S1 and S3 is shown with red respectively green bands and the polepoints are presented by red triangles respectively green diamonds in the stereonet. The yellow bands indicate the position of the hydraulic fractures. The value of the injectivity is indicated before (blue) and after (red) each HF.

in different propagation regimes (i.e. toughness or viscosity dominated) (Savitski & Detournay, 2002), whereby the goal was to achieve similar behavior than for high rate stimulation in EGS projects. During the tests we used water and a rheology modifier to achieve viscosity dominated propagation regime. The latter one consists of xanthan-salt-water (XSW) and has a 35 times higher viscosity than water. Several monitoring systems were installed to study transient pressure propagation, deformation within the rock mass and along shear zones at high spatial and temporal resolution and seismic activities. We present in this paper some preliminary results of our hydro-mechanical data. We focus on the comparison of some characteristic parameters (i.e. injectivity enhancement ratio, jacking pressure and fluid recovery) of each hydraulic fracture and we show distinct fracture propagation behaviors within our experimental volume.

2. GEOLOGICAL SITE DESCRIPTION

The GTS is located in the Central Swiss Alps, around 480 m below ground level. The ISC test volume is located in the southern part of the test site (Fig. 1A). The ISC experimental volume is situated slightly south of the boundary between Central Aare Granite (towards north) and Grimsel Granodiorite (towards south). The moderately fractured rock mass is crosscut by five subvertical ductile and brittle-ductile shear-zones. The first set (referred to as: S1.1, S1.2 and S1.3) included three ductile shear zones that were characterized by a strong increase in the degree of foliation and mylonitization. All three shear zones had an ENE-WSW strike and dip towards SE. The second set (referred to as S3.1 and S3.2) contained two brittle-ductile shear zones. The S3 brittle-ductile shear-zones consists of a densely fractured zone (>20 fractures per meter) in between two biotite-rich meta-basic dykes. The fracture frequency in the INJ boreholes is 0-3 fractures per meter, with higher frequency towards the shear zones. Optical televiewer logging in INJ1 and INJ2 indicated a preferred fracture orientation striking E-W along the main structural features (S1: red triangles; S3: green diamonds) (Krietsch et al., n.d.) (Fig. 2).

During the pre-stimulation phase, the in-situ local stress field was measured by overcoring methods (i.e. USBM and CSIRO-HI probes) and hydraulic fracturing. Impression packers and microseismic monitoring were used to map hydraulic fracture orientation which revealed consistent E-W, subvertical fracture extension. The unperturbed stress field has a minimal principal stress magnitude of 8.6-9.7 MPa and is sub-horizontal N-S oriented. The major principal stress magnitude ranges

between 13.1 – 14.4 MPa and plunges with 30 to 40° to the East. The intermediate stress component ranges from 9.2 to 10.2 MPa. The S3 shear zone perturbs the stress field as the minimal stress component decline towards S3 to 3 MPa (Krietsch et al., 2018).

3. HYDRAULIC FRACTURING

From optical televiewer (OPTV) borehole logging intact intervals were identified for the HF locations in the two injection boreholes INJ1 and INJ2 (Fig. 1C). HF3, HF5, and HF8 were located south of the S3 shear-zones and HF1, HF2, and HF6 were located north of S3 shear-zones. The initial transmissivity was measured by two pulse tests and ranged between 1.4-3.8 10^{-13} m^2/s for all HF intervals. The initial injectivity was estimated from the transmissivity using the steady-state radial flow equation. An injectivity value of 1 (l/min)/MPa corresponds to the transmissivity of 4.42 10^{-8} m^2/s for a wellbore of 0.07 m and a radius of influence of 0.4 m. The initial injectivity of the intact intervals ranged from 3.2 10^{-6} to 8.6 10^{-6} l/min/MPa. All HF experiments took place in intact rock without any fractures in the stimulated interval except HF6, which was accidentally stimulated three meters further down in the injection borehole at an interval with a pre-existing fracture.

3.1. HF procedure

The HF interval was packed off using a hydraulic double-packer system with a base length of 1 m to pressurize the interval with an injection pressure up to 30 MPa. Two different pumps were used to deliver a flow rate up to 100 l/min at a maximal pressure of 10 MPa and a pressure up to 30 MPa at a flow rate up to 35 l/min. A second double-packer system was installed to monitor the pore pressure response in a monitoring interval in the second injection borehole that was not used for active stimulation. Pore pressure was also monitored in the intervals beneath the injection and monitoring intervals. The injected fluid and the flow-back were measured with flowmeters. Once installed, all the packer intervals were saturated with water.

To test the interval integrity and proper packer sealing a pulse test was performed (compare Fig. 3). The actual hydraulic fracturing test started with a controlled rate fluid injection with a rate of approximately 5 l/min for half a minute to initiate a hydraulic fracture. The fracture propagation cycle had the aim to propagate the hydraulic fracture. This propagation cycle was executed in two cycles (C1 and C2) between which the pump was changed and reached a maximum flow rate of 100 l/min. For the tests during which xanthan-salt-water (XSW) was injected, a flushing cycle (C3) was added afterwards. The last cycle was a pressure-controlled cycle (C4) to evaluate the post-stimulation transmissivity of the created hydraulic fracture and to estimate the stress acting normal to the hydraulic fracture (jacking pressure).

Figure 3 shows flow-rate versus injection pressure for the HF3 experiment during different injection cycles. The pressure was read at steady-state flow. During C2 the flow rate exceeds a maximum pressure of 6.8 MPa below 52 l/min. Above 52 l/min, the flow rate was ramped up faster as a consequence the pressure raised, instead keeping it at 6.8 MPa. Final injectivity and jacking pressure were measured during step-pressure cycle (C4). The final injectivity was extracted from the slope of the linear fit through the first six flow rate vs. pressure data points. The linear fit to the last three data points and solving the equation for y=0 gives the jacking pressure.

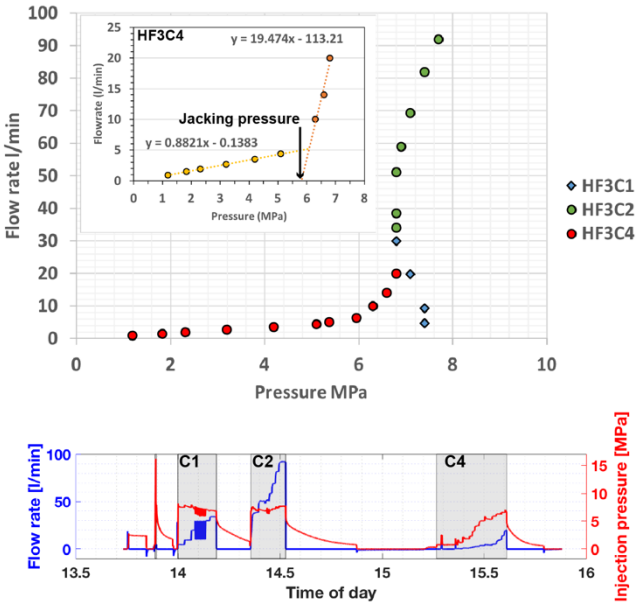

Fig. 3: Flow-rate vs. pressure plot for HF3 experiment divided by fracture propagation cycle 1 (C1) and 2 (C2) and pressure step rate test (C4). The final injectivity and jacking pressure was taken from the pressure step rate cycle.

3.2. Variations along INJ1 and INJ2

The comparison of the injectivity increase, jacking pressure and injection recovery for the different tests (see Table 1) indicate similar results for tests deep respectively shallow in the boreholes. The jacking pressure decreases and fluid recovery in the injection interval increases from the south (shallow borehole depth) to the north (near borehole end). It is noteworthy that the injectivity increase is highest for HF1 and HF2, which are located north of the S3 zone. Highest injectivity after stimulation was measured for HF2 and HF6 with 3.69 resp. 2.77 l/min/MPa. HF3 and HF8 showed similar jacking pressure and injection recovery, but different injectivity enhancement ratio. As there was no back-flow in the injection interval, the fracture near the borehole wall closed directly after shut-in. Note that the injection fluid for HF3 was water, whereas it was XSW for HF8. During these two tests, the fracture was drained to the AU-tunnel via zone S3.1, which consists to the southern boundary of S3 and at the end of propagation cycle 2 the fracture

Table 1: Hydraulic and seismic characteristics of the 6 HF experiments with injection locations highlighted in red (north of S3) and yellow (south of S3) and break down characteristics highlighted in light blue (north of S3) and blue (south of S3).

Test	Bore-hole	Depth [m]	Total Injected Volume [l]	Recovery injection interval [%]	Jacking pressure [MPa]	Total Number of recorded events	Trace description xxx/xx°; depth	Break down [MPa]	Injected volume breakdown cycle [l]	Injection recovery breakdown cycle[%]	ISIP [MPa]
HF1	INJ1	40.5	1565	24.8	2.2	N / A	190/88.1°; 39.5-41.0 m	14.9	1.70	34.7	6.6
HF2	INJ1	36.3	964	28.7	3.3	2204	041.5/88.9°; 35.8-37.1 m	13.95	1.66	100	5.5
HF3	INJ1	20.3	911	2.0	5.8	1997	217.7/86.8° and 217.7/80.3°; 20.1-21.2m	16.3	1.71	100	7.7
HF5	INJ1	14.5	1553	0.3	6.4	1969	205.9/89.2°; 13.8-15.6 m	20.5	1.88	52.1	7.9
HF6	INJ2	38.9	1222	58.4	3.0	94	193.7/87.6°; 39.2-39.9 m	(7.0)	2.08	55.3	5.9
HF8	INJ2	15.7	1142	1.8	5.0	722	209.2/81.9°; 15.8-16.4 m	21.2	1.63	30.7	7.5

connected to the geophysical boreholes. HF5 behaved differently as we hit one of the seismic observation boreholes during the first propagation cycle.

The induced seismicity during hydraulic fracturing experiments was monitored with a dense monitoring network of highly sensitive sensors. The network consisted of 24 piezo-sensors and 6 accelerometers, which were connected to a 32-channel acquisition system with a sampling frequency of 200 kHz. The analysis of seismic data is still in progress and only preliminary results are presented. An initial seismic event count was established by detecting events with a recursive STA/LTA method. The number of recorded events (Table 1) does not show a systematic pattern that depends on the injection below or above S3. The total number of recorded events for HF2, HF3 and HF5 range between 1969 and 2204. Only 94 respective 722 events were recorded for HF6 resp. HF8.

3.3. Break down analysis

The break down pressure and the instantaneous shut-in pressure (ISIP) during breakdown cycle (Table 1) range between 7.0 to 21.2 MPa respective between 5.5 to 7.9 MPa. The ISIP ranges between 7.5 and 7.9 MPa for HF locations south of S3 shear zones and decreased to 5.5 - 6.6 MPa toward the north. The behavior for the breakdown varied more in magnitude. Nevertheless, breakdown pressure north of S3 were smaller than 15 MPa and larger than 16 MPa south of S3. No real breakdown was observed during HF6 with a break down pressure of only 7.0 MPa. The total injected volume during breakdown cycle ranged between 1.63 and 2.78 l, with an injection recovery ranging between 30.7 to 100%. The full recovery during breakdown cycles can have two reasons. Either a natural, saturated fracture was hit during break down cycle or the saturation of the intervals or the tubing was inadequate. The initialized fractures were identified along the borehole wall using acoustic televiewer (ATV) borehole logging. Most hydraulic fractures were initiated as axial fractures. A sinusoidal fit was used to estimate dip and dip direction. The fracture trace length ranged from 0.57 m to 1.8 m.

The orientation of the new initiated hydraulic fractures are in good agreement i) with the observations from HF traces in SBH1 and ii) with the microseismic cloud. The normal point to the microseismic cloud corresponds to the minimal principal stress axis σ_3 at 005/15° (Gischig et al., 2018; Krietsch et al., 2017).

4. FRACTURE GEOMETRY

A comparison of the rock mass conditions and transient pressure response on HF2 (north of S3) and HF3 (south of S3) is done in the following, to study the geometry of the newly created fractures and the interaction of natural fractures. In total, 12 pressure observation intervals to observe pressure evolution and 60 fibre-Bragg grating (FBG) sensors with 1 m base length, high sampling rate (1 kHz) and high resolution (0.1 $\mu\epsilon$) were installed to observe the rock mass deformation.

4.1. HF3

The three FBG sensors presented in Fig. 4a are positioned across pre-existing natural fractures. During break down cycle a small extensive strain response of approximately 5 $\mu\epsilon$ was observed in the FBG sensor at a radial distance of 3.7 m in FBS2 to the injection point (Fig. 4a, not visualized). The strain sensor at 3.7 m in FBS1 reached a magnitude of 300 $\mu\epsilon$ and the sensor at 3.7 m in FBS2 a magnitude of 700 $\mu\epsilon$ during the first propagation cycle. The sensor at 4.5 m started to show tension, where the sensor at 3.7 m (FBS2) indicated closing again. At the same time, the interval pressure in PRP13 showed strong variations. We interpret that these pressure oscillation are associated with an episodic stick-split mechanism as

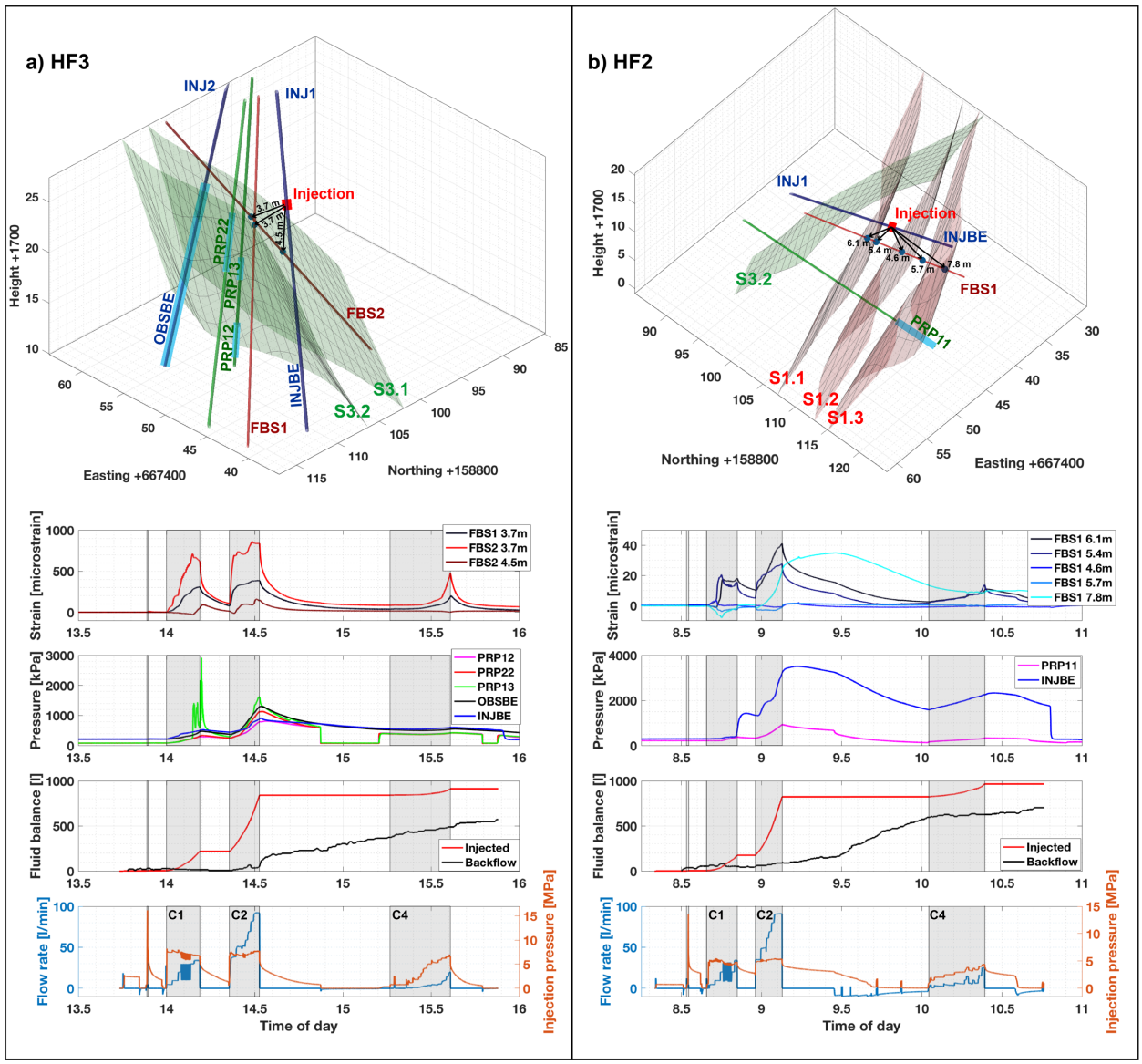

Fig 4: The comparison study between HF3 (south of S3) and HF2 (north of S2) compares most important rock mass response (strain plot), transient pressure propagation (pressure plot), fluid balance and flow rate (blue line) respective injection pressure (red line). The presented strain (tension is positive) and interval pressures respond positively to fluid injection (grey shaded areas). The 3D models include the boreholes with sensor/interval positions, injection point, and the major geological features.

proposed by van der Baan et al. (2016). Further analyses with the integration of the seismic data will give more insight into this response.

In the second propagation cycle (C2), the observed strain and pressure exceeded the values from the first propagation cycle. The pressure intervals shown in Fig. 4a are known to be open flow path connections, as observed during the pre-characterization phase using conductivity logging (Jalali et al., 2018). A direct connection exists between the pressure interval below injection (INJBE) and the pressure interval below observation (OBSBE). An increase in pressure was observed in interval PRP12, PRP13, and PRP22. This is either due to transient pressure response or direct flow path connection. The pressure observation during hydraulic fracturing indicated pressure increase in all of these intervals. We observed generally a short delay time, which is in agreement with the assumption of direct fluid flow, due to the hydraulic fractures. The interval react in the following order: PRP13, then PRP22 and OBSBE and finally PRP12 and INJBE. This is controlled by the flow path through the new created and connected fracture system and reflects pressure diffusion through this system.

The small injection recovery of only 2.0% from the injection interval and the instantaneous pressure decay below jacking pressure after shut-in during propagation cycle 2 (C2) indicates that the injected fluid is not confined in the rock mass and found alternate escape way to the tunnels (zero pressure boundary) through the S3

shear zones. This also might explain the closing of the fracture near the injection borehole. In total, 840 l was injected until shut-in of C2. Before the shut-in of C2, 11% of total injection fluid was already drained toward the tunnel. This drained volume increased to 31% of total injected volume until bleed-off. We continued the HF protocol without waiting for full recovery. At the end of monitoring (~100 min after C2 shut-in), two third of the injected fluid had drained to the tunnel. This indicates that the densely fractured zone in S3 was able to drain most of the fluid towards the AU tunnel, which can be seen by the linear increase in the backflow volume.

4.2. HF2

The FBG strain sensor with a distance of 5.4 m in FBS1 to the injection point responded at a flow rate of 5 l/min (Fig. 4b) during the first fracture propagation cycle (C1). The FBG sensors' responses next to the injection point are shown in the time-strain plot of Fig. 4b. The maximum recorded strain is about 40 $\mu\epsilon$ which is in comparison only about one-tenth of the maximum strain magnitude observed during HF3. During C1, the sensors at 6.1 and 5.4 m indicated opening while sensors at 5.7 and 7.8 m show closing. The pressure monitoring points in the rock mass do not show an increase during the first fracture propagation cycle. Only shortly before shut-in of C1, the INJBE interval starts to increase up to 1.4 MPa during the shut-in phase.

During the second propagation cycle (C2), the FBG sensor at 7.8 m starts closing before it opens at the same time than the pressure in INJBE starts to increase. Open flow paths were investigated by conductivity logging before hydraulic fracturing with a low respond in pressure in the interval PRP11, injecting from the INJBE interval (Jalali et al., 2018). This indicates a transient pressure change in the vicinity without any direct flow path to PRP11. In addition, the pressure interval INJBE exceeded pressure above 3 MPa with a response delay in shut-in and the PRP11 interval increased to a maximum value of 0.9 MPa without a delay in response during shut-in.

About 30% of the injected fluid is recovered through the injection interval compared to 2% during the HF3 test. In total at the end of the test (~100 min after C2 shut-in), 73% of the injected fluid was recovered. The other distinctive features of this test is a small jacking pressure and a large injectivity increase. We interpret these observations as reflecting 1) stress perturbation in the vicinity of the S1 shear zones and 2) connection of the HF with the S1.1 and S1.3 shear zones (Fig. 4b) resulting in the stimulation of these pre-existing zones. The system, however, stayed almost closed, i.e. direct drainage to the tunnel was very limited.

4.3. Outlook

In our future work, we plan to quantify in more detail the fracture geometry in terms of fracture height and length, using the volume balance and AE localization. The localized AE events are necessary to evaluate the fracture geometry and to track the fluid flow. The response of transient pressure and FBG strain data will be compared to each flow rate step to investigate hydromechanical processes. Combining the 3D strain and pressure data allows estimating fracture aperture changes and transmissivity in the vicinity of the injection location. Additionally, longitudinal strain from FBG sensors along with recordings at three tiltmeters can be used to infer the fracture geometry.

5. CONCLUSION

The initial analysis of our HF tests shows two distinct responses in our suite of tests: a different behavior was observed in tests performed south of S3 compared to tests performed north of the S3 shear zone. The main differences are jacking, breakdown and ISIP pressures (low north of S3 and high south of it), fluid recovery through the injection hole (high north of S3, low south of S3), injectivity enhancement ratio (high north of S3 and low south of S3) and strain magnitude recorded during injection (low north of S3 and high south of S3). In the current state of our analyses, we assume that these differences are due to 1) different stress conditions north and south of S3 and 2) different pressure boundary conditions due to the flow path and links to the AU tunnel.

For the experiments HF3 and HF8 (south of S3), the injected fluid was drained by the densely fractured S3 zone towards the AU tunnel. Due to this preferential flow path, the injections took place in an open system. This configuration also favored direct flow connections reflected by instantaneous responses of some pressure monitoring intervals to our injection and high-pressure levels recorded in the intervals.

During the injection north of S3 (i.e. HF2) the FBG strain sensors showed only small magnitude responses. The reason for this is not fully understood at the moment and could be related to the stress conditions north of S3 reflected by smaller jacking pressure and ISIP. The stress perturbation can have various reasons, including effects of pre-existing fractures in the shear zones S1, stiffness difference of meta-basic dykes compared to the host rock in S3, and the combination of both effects. In addition, for the injections north of S3, it seems that the HF tests mostly interact with the S1 shear zones in a closed system as most of the injected fluid is recovered later on through the injection borehole.

These differences in behavior seems also to affect the stimulation efficiency of the injections as the injection north of S3 lead to higher injectivity increase ratio. The

reasons for this will be further investigated by integrating the microseismic data in our analyses.

ACKNOWLEDGEMENT

Funding for this project was provided by the Swiss commission for technology and innovation (CTI), EKZ Zürich and Shell through the Swiss Competence Center for Energy Research – Supply of Electricity (SCCER-SoE). Additionally, this project was funded by the SNF-project 200021_165677/1. We are indebted to Nagra for hosting the ISC experiment in their GTS facility and to the Nagra technical staff for onsite support. We thank MeSy Solexperts, Bochum (Germany) for their good collaboration.

REFERENCES

Amann, F., et al. (2018). The seismo-hydro-mechanical behaviour during deep geothermal reservoir stimulations : open questions tackled in a decameter- scale in-situ stimulation experiment. *Solid Earth*, *9*(August), 115–137. https://doi.org/https://doi.org/10.5194/se-9-115-2018

Cummings, R.G., Morris, G.E., Tester, J.W., & Bivins, R.L., (1979). *Mining earth's heat: hot dry rock geothermal energy*. United States.

Der Baan, M. van, Eaton, D. W., & Preisig, G. (2016). Stick-split mechanism for anthropogenic fluid-induced tensile rock failure. *Geology*, *44*(7), 503–506. https://doi.org/10.1130/G37826.1

Detournay, E. (2016). Mechanics of Hydraulic Fractures. *Annual Review of Fluid Mechanics*, *48*(1), 311–339. https://doi.org/10.1146/annurev-fluid-010814-014736

Eaton, D. W., & Igonin, N. (2018). What controls the maximum magnitude of injection-induced earthquakes? *The Leading Edge*, *37*(2), 135–140. https://doi.org/10.1190/tle37020135.1

Evans, K. F., Zappone, A., Kraft, T., Deichmann, N., & Moia, F. (2012). A survey of the induced seismic responses to fluid injection in geothermal and CO2 reservoirs in Europe. *Geothermics*, *41*, 30–54. https://doi.org/10.1016/j.geothermics.2011.08.002

Gischig, V., & Preisig, G. (2015). Hydro-fracturing versus hydro-shearing: a critical assessment of two distinct reservoir stimulation mechanisms, (September 2016). https://doi.org/10.13140/RG.2.1.4924.3041

Gischig, V. S., et al. (2018). On the link between stress field and small-scale hydraulic fracture growth in anisotropic rock derived from microseismicity. *Solid Earth*, *9*(1), 39–61. https://doi.org/10.5194/se-9-39-2018

Jalali, M., et al. (2018). Transmissivity Changes and Microseismicity Induced by Small-scale Hydraulic Fracturing Tests in Crystalline Rock. *Geophysical Research Letters*, 45. https://doi.org/10.1002/2017GL076781

Jalali, M., et al. (2018). A Multi-Scale Approach to Identify and Characterize the Preferential Flow Paths of a Fractured Crystalline Rock. In *2nd International DFNE Conference*, 2018-0734, Seattle.

Jeffrey, R. G., et al. (2009). Measuring Hydraulic Fracture Growth in Naturally Fractured Rock. *SPE Annual Technical Conference and Exhibition*, 1–19. https://doi.org/10.2118/124919-MS

Krietsch, H., Doetsch, J., Dutler, N. O., Jalali, M., Gischig, V. S., Loew, S., & Amann, F. (n.d.). Comprehensive geological data of a fractured crystalline rock mass analog for hydraulic stimulation experiments. *(Submitted to Nature scientific data)*.

Krietsch, H., et al.(2018). Stress measurements for an in-situ stimulation experiment: Integration of induced seismicity, stress relief and hydraulic methods in crystalline rock. *(Submitted to Rock Mechanics and Rock Engineering)*.

Krietsch, H., Gischig, V., Jalali, M. R., Amann, F., Evans, K. F., Doetsch, J., & Valley, B. (2017). Stress measurements in crystalline rock : Comparison of overcoring, hydraulic fracturing and induced seismicity results. *American Rock Mechanics Association*.

López-Comino, J. A., Cesca, S., Heimann, S., Grigoli, F., Milkereit, C., Dahm, T., & Zang, A. (2017). Characterization of Hydraulic Fractures Growth During the Äspö Hard Rock Laboratory Experiment (Sweden). *Rock Mechanics and Rock Engineering*, (August), 1–17. https://doi.org/10.1007/s00603-017-1285-0

Manning, C. E., & Ingebritsen, S. E. (1999). Permeability Implications of the Continental of Geothermal Data Crust and Metamorphic Systems. *Reviews of Geophysics*, *37*(1), 127–150.

McClure, M. W., & Horne, R. N. (2014). An investigation of stimulation mechanisms in Enhanced Geothermal Systems. *International Journal of Rock Mechanics and Mining Sciences*, *72*, 242–260. https://doi.org/10.1016/j.ijrmms.2014.07.011

Pine, R. J., & Batchelor, A. S. (1984). Downward migration of shearing in jointed rock during hydraulic injections. *International Journal of Rock Mechanics and Mining Sciences and*, *21*(5), 249–263. https://doi.org/10.1016/0148-9062(84)92681-0

Rutqvist, J., & Stephansson, O. (2003). The role of hydromechanical coupling in fractured rock engineering. *Hydrogeology Journal*, *11*(1), 7–40. https://doi.org/10.1007/s10040-002-0241-5

Savitski, A. A., & Detournay, E. (2002). Propagation of a penny-shaped fluid-driven fracture in an impermeable rock: Asymptotic solutions. *International Journal of Solids and Structures*, *39*(26), 6311–6337. https://doi.org/10.1016/S0020-7683(02)00492-4

Warpinski, N. R. (1985). Measurement of width and pressure in a propagating hydraulic fracture. *Society of Petroleum Engineers Journal*, *25*(1), 46–54.

Zang, A., et al. (2017). Hydraulic fracture monitoring in hard rock at 410 m depth with an advanced fluid-injection protocol and extensive sensor array. *Geophysical Journal International*, *208*(2), 790–813. https://doi.org/10.1093/gji/ggw430